Lithium-Ion Batteries

DOI: 10.1002/anie.201408853

Hierarchical Surface Atomic Structure of a Manganese-Based Spinel Cathode for Lithium-Ion Batteries**

Sanghan Lee, Gabin Yoon, Minseul Jeong, Min-Joon Lee, Kisuk Kang, and Jaephil Cho**

Abstract: *The increasing use of lithium-ion batteries (LIBs) in high-power applications requires improvement of their high-temperature electrochemical performance, including their cyclability and rate capability. Spinel lithium manganese oxide ($LiMn_2O_4$) is a promising cathode material because of its high stability and abundance. However, it exhibits poor cycling performance at high temperatures owing to Mn dissolution. Herein we show that when stoichiometric lithium manganese oxide is coated with highly doped spinels, the resulting epitaxial coating has a hierarchical atomic structure consisting of cubic-spinel, tetragonal-spinel, and layered structures, and no interfacial phase is formed. In a practical application of the coating to doped spinel, the material retained 90% of its capacity after 800 cycles at 60 °C. Thus, the formation of an epitaxial coating with a hierarchical atomic structure could enhance the electrochemical performance of LIB cathode materials while preventing large losses in capacity.*

Spinel lithium manganese oxide ($LiMn_2O_4$) is being spotlighted as a promising cathode material for lithium-ion batteries (LIBs) for electric vehicles and energy-storage systems owing to its low cost, high abundance, high safety, nontoxicity, high operating voltage, and excellent rate capability.[1] However, $LiMn_2O_4$ exhibits severe capacity fading upon cycling and after storage, especially at elevated temperatures (> 60 °C).[2]

Many researchers have attempted to elucidate the capacity-fading mechanism of 4V $LiMn_2O_4$. The suggested mechanisms can be broadly classified as follows: dissolution of Mn^{2+} in the electrolyte[3] ($2\,Mn^{3+}{}_{solid} \rightarrow Mn^{4+}{}_{solid} + Mn^{2+}{}_{electrolyte}$) and continuous decomposition of the electrolyte at high voltages.[4] To overcome these disadvantages, the following techniques have attracted most attention, as they can be implemented in a straightforward manner at low cost: 1) the partial cationic substitution of manganese with other metals, so that the average oxidation state remains higher than 3.5 and the structural stability is improved owing to the strong metal–oxygen bonds formed by the substituted metal ions ($LiM_xMn_{2-x}O_4$, M = Li,[5] Co,[6] Mg,[7] Ni,[8] Al,[9] or Zn);[1b] 2) the use of a metal-oxide (Co_3O_4,[10] Al_2O_3,[11] ZnO,[12] MgO,[13] or SiO_2)[14] surface coating and control of the particle size to reduce the electrochemically active surface area between the active material and the electrolyte, thus preventing undesirable reactions at the interface.

In the last two decades, the high-temperature lifespan of manganese-based spinel cathodes has been increased markedly by using these methods. However, the degree of doping cannot be increased more than a certain extent, because of the trade-off between the doping level and the gravimetric capacity.[15] Similarly, the surface of the active material cannot be fully covered by the metal-oxide coating. The coating coverage can be improved by increasing the amount of the coating material, but several disadvantages are observed as result, such as a reduction in capacity and an increase in ionic resistance. Therefore, the formation of an electrochemically active coating layer on the host material could be highly effective in improving its electrochemical performance without sacrificing its high capacity. Furthermore, the expectation is that a protective layer and a HF scavenger should form at the interface. However, in previously reported studies, numerous changes were induced in the electrochemical properties of the host material when it was covered with a metal-oxide coating.[16] These changes in the electrochemical properties may result from changes in the surface structure of the host material during the coating process, because surface-coating methods involve high-temperature calcination of the material. It is possible that the metal ions in the coating material, including those of Co, Al, and Mg, diffuse into the host material, thus changing its electrochemical behavior. Therefore, it is necessary to elucidate the effect of the protective layer and that of the surface-structure modification of host materials to understand the role of surface coatings. However, it was very difficult to determine whether the improvements in the electrochemical properties of the host material are attributable to the physical coating or to the surface-structure modification.

Herein, we report the application of a highly doped $Li_{1+x}Mn_{2-x-y-z}Al_yMg_zO_4$ coating on stoichiometric $LiMn_2O_4$ without the formation of an interfacial phase and the

---

[*] Dr. S. Lee, M. Jeong, M. Lee, Prof. J. Cho
School of Energy and Chemical Engineering
Ulsan National Institute of Science and Technology (UNIST)
689-798, Ulsan (Republic of Korea)
E-mail: jpcho@unist.ac.kr

G. Yoon, Prof. K. Kang
Department of Materials Science and Engineering, Research Institute of Advanced Materials (RIAM), Seoul National University
Gwanak-ro 599, Gwanak-gu, Seoul 151-742 (Republic of Korea)
and
Center for Nanoparticle Research
Institute for Basic Science (IBS), Seoul National University
Gwanak-ro 599, Gwanak-gu, Seoul 151-742 (Republic of Korea)
E-mail: matlgen1@snu.ac.kr

[**] This research was supported by the Secondary Battery R&D Program for Leading Green Industry from the MOTIE/KEIT [10042840, development of LMO cathode materials of high capacity (≥ 120 mAh g^{-1}) and high density (≥ 2.0 g mL^{-1}) for EV] and by IBS-006-D1.

Supporting information for this article is available on the WWW under http://dx.doi.org/10.1002/anie.201408853.

investigation of the effects of changes in the surface microstructure of $LiMn_2O_4$ on its electrochemical properties. By the use of scanning transmission electron microscopy (STEM), it was determined that the coating precursors, consisting of a mixture of Mn, Al, Mg, and Li, were completely incorporated into the bulk phase on the surface to form an epitaxial layer. This complete incorporation prevented the formation of an interfacial phase and facilitated the formation of a protective layer; no inactive materials were present on the particle surfaces.

The coated material exhibited improved electrochemical performance, including greater rate capability and capacity retention at an elevated temperature. These improvements are attributed to the reduction in the activation energies of the charge-transfer reaction at the surface and of lithium-ion diffusion in the host material, the high mean oxidation state of manganese ions at the surface, the formation of a stable manganese-based layered structure near the surface, and the formation of a tetragonal buffer zone with respect to microstrains at the surface of particles during fast discharging.

We synthesized stoichiometric $LiMn_2O_4$ microparticles with an average particle size of 6 μm. These particles were then used to fabricate the two active materials evaluated in this study: 1) They were coated sequentially with $Li_{1.15}Al_{0.32}Mn_{1.53}O_4$ and $Li_{1.15}Mg_{0.2}Mn_{1.65}O_4$ by spray drying and subsequent firing (spinel-coated $LiMn_2O_4$, SLMO; see Figure S1 in the Supporting Information). Assuming that the coating precursors were completely consumed in the reactions to form $Li_{1.15}Al_{0.32}Mn_{1.53}O_4$ and $Li_{1.15}Mg_{0.2}Mn_{1.65}O_4$, we estimated the coating amounts at 5 wt % of the bare sample. 2) The initial particles were also fired in the same manner as the coated particles to eliminate the calcination effects on its electrochemical properties (bare $LiMn_2O_4$, BLMO).[17] Commercial $Li_{1+x}Mn_{2-x-y}M_yO_4$ has a capacity of approximately 105 $mA\,h\,g^{-1}$ owing to its high doping level, whereas the theoretical capacity of $LiMn_2O_4$ is 148 $mA\,h\,g^{-1}$. Our goal was to form a very stable surface on high-capacity $LiMn_2O_4$ without affecting its electrochemical performance, including its rate capability. In this regard, highly doped $Li_{1+x}Mn_{2-x-y}M_yO_4$ is a very attractive material for modifying the surface of $LiMn_2O_4$ owing to its high cyclability, high lithium-ion conductivity, and possible contribution to capacity.

The X-ray diffraction (XRD) patterns of BLMO and SLMO exhibited no impurity phases, and all peaks could be assigned to cubic spinel ($Fd\bar{3}m$; see Figure S2). The only difference in the structures of BLMO and SLMO was in the lattice parameter, and this difference was small. The lattice parameters of BLMO and SLMO were 8.2386 and 8.2296 Å, respectively. However, the coating materials $Li_{1.15}Al_{0.32}Mn_{1.53}O_4$ and $Li_{1.15}Mg_{0.2}Mn_{1.65}O_4$ have a lattice parameter of approximately 8.15 Å; furthermore, the total amount of the coating materials in the host was almost 10 wt %. Therefore, the XRD patterns of the coating materials could be distinguished from that of the host material, thus indicating that the coating materials and the host material formed a solid solution.

The first discharge capacity of BLMO and SLMO was approximately 130 and 122 mA h g−1, respectively (see Figure S3 a). The normalized voltage profiles of BLMO and SLMO (see Figure S3 b) were almost identical at voltages of 3–4.05 V, whereas the curves at voltages of 4.05–4.3 V were slightly distinct. Ohzuku et al. reported that the reaction consists of one cubic phase ($a_{cubic} = 8.24$–8.14 Å) at 3.94 V and two cubic phases ($a_{cubic} = 8.14$ Å, $a_{cubic} = 8.03$ Å) at 4.11 V.[18] In the voltage range of 4.05–4.3 V, BLMO showed the flat voltage plateau of a two-cubic-phase reaction ($Li_{0.5}Mn_2O_4$–λ-MnO_2) accompanied by sudden changes in the lattice parameter. On the other hand, the curve for SLMO had a nearly smooth slope, thus indicating a reaction with a single cubic phase and a gradual change in the lattice parameter.

The chemical composition of SLMO was $Li_{1.087}Mn_{1.888}Al_{0.014}Mg_{0.011}O_4$, as determined by inductively coupled plasma atomic emission spectrometry (ICP-AES), thus indicating that the theoretical capacity of SLMO should be only 113 $mA\,h\,g^{-1}$. SLMO exhibited a gravimetric capacity of more than 120 $mA\,h\,g^{-1}$. Thus, the difference in the two capacities was very small. However, the practical capacity of a material is usually only 90 % of its theoretical capacity. For SLMO, a higher capacity was observed because it was heterostructured.

Energy-dispersive X-ray spectroscopy (EDX) showed that the Al concentration in the spinel structure at the surface of secondary particles was high; this high Al concentration positively affected the cyclability of $LiMn_2O_4$ by suppressing side reactions (Figure 1 b–d). Dry coating methods and

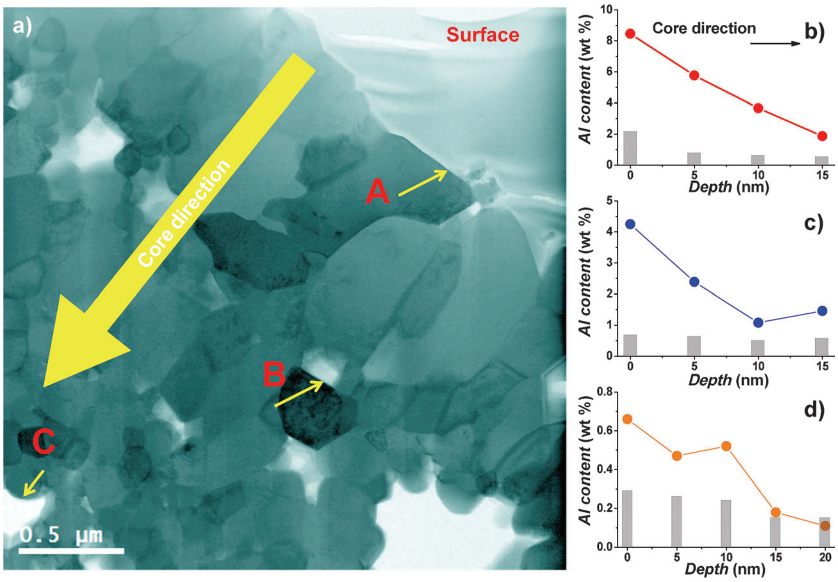

Figure 1. HRTEM image of SLMO. The secondary particles consisted of aggregates of primary single particles with a broad size distribution (ca. 50 nm–1 μm) and had a number of pores. a) HRTEM cross-sectional image of SLMO. b–d) EDX point analysis of primary particle A (b), B (c), and C (d) along the thickness direction from the surface to the core (the bars indicate the errors for the EDX analysis).

colloidal coating methods usually focus only on the surfaces of the secondary particles. However, the electrolyte can penetrate between the secondary particles during cycling. Therefore, it is necessary to introduce a stable inner surface. However, in the fabricated samples, Al atoms were observed both on the surfaces of the primary particles and within the secondary particles (Figure 1 b–d). The Al content on the surface of three primary particles (points A, B, and C in Figure 1) was approximately 9, 4, and 0.7 wt %, respectively. Furthermore, a gradient existed in the Al concentrations between the particle surface and the core for both the secondary particles and the inner primary particles, thus indicating that this coating method could cover the surfaces of the inner primary particles as well as those of the secondary particles. Moreover, the decrease in capacity observed after coating was minimized because the substituted Al atoms were concentrated at the surfaces of the primary particles, particularly in the case of particles close to the surface of the secondary particles. Although the Mg atoms were not detected by EDX owing to their low mass concentration, we believe that they should show a similar concentration gradient to the Al atoms because the coating procedure was the same. Hence, SLMO exhibited a capacity higher than its theoretical capacity of 113 $mA\,h\,g^{-1}$.

In the $LiMn_2O_4$ structure, the oxygen atoms are in a face-centered-cubic close-packing arrangement, which results in tetrahedral and octahedral vacancies for Li ions (8a) and Mn ions (16d), respectively. The tetrahedral and octahedral sites have occupancies of one-eighth and one-half, respectively. This arrangement results in a three-dimensional network of edge-shared MnO_6 octahedra. The formula for $LiMn_2O_4$ with a spinel structure can be written as $[Li^+]_{8a}[Mn^{3+}\text{-}Mn^{4+}]_{16d}[\square]_{16c}[O_4]_{32e}$ with the space group $Fd\bar{3}m$ (□ represents the vacancies). In Figure 2 e, the difference between the Mn_α and Mn_β columns is in the number of Mn ions per unit length; Mn_α has a Mn density that is twice than that of Mn_β. The long diagonal is 0.824 and corresponds to the lattice parameter. The difference in contrast of the Mn_α and Mn_β columns can be seen clearly in region I (Figure 2 a,b). Interestingly, the coating layers in regions II and III grew epitaxially on SLMO by sharing the cubic-close-packed (ccp) oxygen crystal axis. All metal ions were in a row; however, the site occupancies of the metal ions in regions II and III were different. In region II, there was no difference in the brightness of the Mn_α and Mn_β columns, and a new metal column was generated at the center of the rhombus. This region corresponds to the layered structure ($R\bar{3}m$, $[2\bar{2}1]_{trigonal}$; Figure 2 f). The random distribution of the columns indicates that the layered structure has a number of metal vacancies. That is to say, cation mixing with Li ions occurred. Region III exhibited the usual differences in brightness; however, a new metal column was also generated at the Li site. When viewed in combination with the EDX results (Figure 1), this new metal column must be formed by Mn, Al, or Mg ions; it is unlikely that it is formed by a light element, such as Li or O, as the electron-beam-scattering capability of such elements is weak. Therefore, region III corresponds to the tetragonal structure ($I4_1/amd$, $[100]_{tetragonal}$; Figure 2 d,g; see also Figure S7).

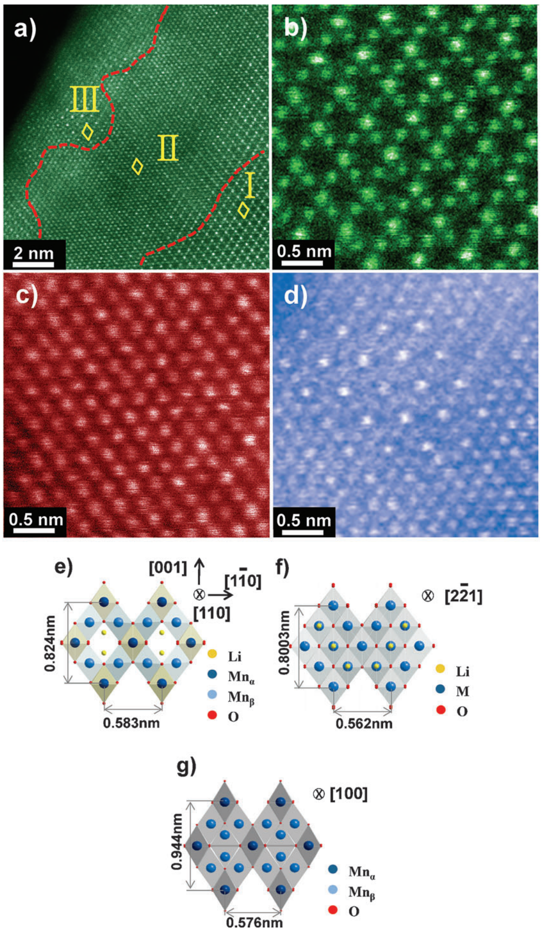

Figure 2. a) HAADF-STEM image of SLMO (surface image of particle A in Figure 1) in the $[110]_{cubic}$ direction. b) Region I in (a) corresponds well to the spinel structure of $LiMn_2O_4$. c) In region II, a new metal column was observed at the center of each rhombus; there was no difference in the brightness of the columns. d) In region III, a few metal columns were observed at the Li site (8a); their brightness was comparable to that of the Mn_β columns. The image contrast is roughly proportional to the atomic number Z and the number of metal atoms in a particular column. e–g) Schematic illustration of the crystal structure of $LiMn_2O_4$ viewed from the $[110]_{cubic}$ direction (e), the layered cathode material ($LiCoO_2$) viewed from the $[2\bar{2}1]_{trigonal}$ direction (f), and tetragonal Mn_3O_4 viewed from the $[100]_{tetragonal}$ direction (g). The polyhedra indicate the MnO_6 octahedra, and Li, Mn, and O are represented by spheres. The white center consists of the 8a and 16c sites and forms a lithium-ion-diffusion pathway along 16c→8a→16c→8a through sharing of the faces.

Recently, we were able to fabricate a $LiNi_{0.5}Mn_{0.5}O_2$ coating on $LiMn_2O_4$ that resulted in heterostructured $LiMn_2O_4$.[16b] We found that the tetragonal Mn_3O_4 phase was an intermediate phase during the formation of a layered structure. However, in the present case, the EDX results suggested that a $[Mg^+]_{8a}[Al^{3+}Mn^{3+}]_{16d}[\square]_{16c}[O_4]_{32e}$ microstructure can be formed in the spinel structure of the host $LiMn_2O_4$. The substituted metal ions of the coating precursor were involved in the formation of the microstructures of the spinel material ($Li[Mn_{2-x-y}Al_xMg_yLi_z]O_4$), the tetragonal-like material ($Mg[MnAl]O_4$), and the layered material ($Li[Mn_{1-x-y}Al_xMg_y]O_2$). For the layered structure, it is wellknown that layered $LiMnO_2$ has the space group $C2/m$ because of the Jahn–Teller effect of Mn^{3+}. It was very hard to clearly differentiate the space group $C/2m$ from $R\bar{3}m$ by STEM analysis. However, on the basis of previous reports, we believe that the layered structure in Figure 2 is close to $C2/m$ rather than $R\bar{3}m$. These phenomena, namely, the formation of layered ($R\bar{3}m$ and $C2/m$) and tetragonal-spinel ($I4_1/amd$) microstructures with the $Fd\bar{3}m$ space group, are possible because these structures are a subgroup of the $Fd\bar{3}m$ space group and all have a cubic-close-packed array of oxygen atoms. Therefore, they can be viewed as hierarchical atomic structures.

Since $LiMnO_2$ exhibits orthorhombic symmetry as the most stable structure,[19] we determined the feasibility of the formation of monoclinic layered ($C2/m$) $LiMnO_2$ by performing first-principles calculations. We first compared the ground-state energies of the two $LiMnO_2$ structures (Figure 3 a). Orthorhombic $LiMnO_2$ is clearly more stable than monoclinic $LiMnO_2$ by 30 meV per formula unit. However, in our case, the doping effects of Mg and Al ions should be considered. Therefore, we next compared the ground-state energies of orthorhombic and monoclinic $LiAl_xMn_{1-x}O_2$ ($x =$ 0.0625, 0.125, 0.25). Figure 3 a shows the relative formation energies of the monoclinic phase as compared to the orthorhombic phase. It is clear that the monoclinic phase became stable as the doping concentration increased. Even though the orthorhombic phase is calculated to be stable at a low Al concentration, the difference in the formation energy is only about 20 meV per formula unit, which is lower than the room-temperature thermal energy (ca. 26 meV). Therefore, the formation of the monoclinic phase is plausible even at small Al concentrations. At our maximum doping concentration, the monoclinic structure became more stable than the orthorhombic structure by approximately 50 meV per formula unit, in agreement with the results reported by Mishra and Ceder.[19] This phenomenon is related to the stability of antiferromagnetic ordering in orthorhombic $LiMnO_2$. The substitution of nonmagnetic metals, such as Al and Mg, disrupts the antiferromagnetic arrangement of Mn^{3+} ions (which helps to stabilize orthorhombic $LiMnO_2$), thus lowering the relative formation energy of monoclinic $LiMnO_2$.[19] Therefore, we can conclude that the formation of monoclinic, layered $LiMnO_2$ is possible in the presence of other cations, such as Al and Mg.

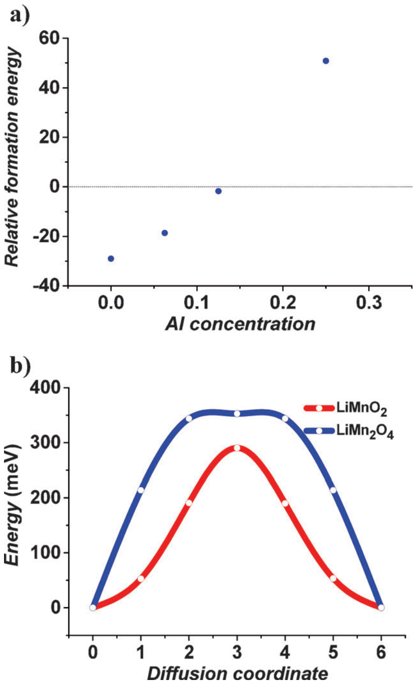

Figure 3. First-principles calculations. a) Relative formation energy of monoclinic $LiMnO_2$ and orthorhombic $LiMnO_2$ at various aluminum-doping concentrations. b) Lithium-diffusion barrier in $LiMn_2O_4$ and monoclinic $LiMnO_2$; the activation barrier to Li^+ diffusion is approximately 20% lower in monoclinic $LiMnO_2$.

The electrochemical properties of the electrode materials used in LIBs are strongly dependent on their structure, because the transfer of Li ions is determined by the crystal structure and coordination geometry of the electrode material. Thus, the microstructure of the epitaxial coating can affect the electrochemical characteristics of the underlying material in several ways. It can act as a protective layer that reduces direct contact between $LiMn_2O_4$ and the electrolyte; this is not the case with SLMO because most of the exposed facets of SLMO are active. Furthermore, it can alter the behavior of Li ions at the electrode/electrolyte interface.

To investigate the lithium-ion-transfer mechanism, we performed electrochemical impedance spectroscopy (EIS) measurements at temperatures ranging from 30 to −20 °C (see Figure S8). At room temperature, the cell resistance of BLMO and SLMO was approximately 7 and 10 Ω. The resistance at a specific temperature is largely determined by the cell conditions, such as the uniformity of electrodes. However, the temperature dependency of the resistance hardly depends at all on the cell conditions. The activation energies (E_a) for the various elements in terms of resistance to Li^+ transport through the solid-electrolyte interphase (R_{SEI}), electric resistance R_e, and charge-transfer resistance (R_{ct}) were calculated from the Arrhenius plots (see Figures S9 and S10). For SLMO, the activation energies in terms of R_{SEI}, R_e, and R_{ct} were 0.16, 0.57, and 0.27 eV, whereas those for BLMO were 0.38, 0.56, and 0.48 eV, respectively. Similarly, at room temperature, the diffusion coefficients of SLMO and BLMO were 6.1×10^{-11} and $5.1\times10^{-11}\,cm^2s^{-1}$, respectively. Moreover, the lithium-diffusion activation energies of BLMO and SLMO were 0.45 and 0.34 eV, respectively; thus, the activation energy of SLMO was found to be 24% lower than that of BLMO (see Figure S10).

To explain the improved kinetic properties of SLMO, we calculated the lithium-diffusion activation barriers for both monoclinic $LiMnO_2$ and spinel $LiMn_2O_4$ (Figure 3 b). In monoclinic layered $LiMnO_2$, the Li ions have to overcome an activation barrier of 290 meV to migrate to other sites, whereas this barrier is 350 meV in spinel $LiMn_2O_4$; these values agree with those reported previously.[20] Similar results are obtained after a small amount of Al is introduced (see Figure S11). Li ions which migrate adjacent to Al ions need to overcome an activation barrier of only 195 meV in layered $LiMnO_2$, whereas 335 meV is required in $LiMn_2O_4$. The activation barrier is lower for $LiMnO_2$ because of the coulombic repulsion between the Li and Mn ions. The oxidation state of Mn in $LiMnO_2$ is 3+, whereas Mn exists in a mixed state of 3+ and 4+ in spinel $LiMn_2O_4$. Therefore, the repulsion between migrating lithium ions and transition-metal ions is weaker in $LiMnO_2$, thus leading to a lower activation barrier. Our results may seem unreasonable because spinel-like $LiMn_2O_4$ has a three-dimensional lithium-ion-migration path, whereas layered $LiMnO_2$ has a two-dimensional migration path, and because the difference in the activation barriers is not large enough to cause an increase in the rate capability. However, Xu and Meng[20a] have shown that the lithium-diffusion activation barrier in the spinel structure could be increased to about 600 meV, depending on the charge states of the surrounding Mn ions. They claim that an increase in the number of surrounding Mn^{3+} ions leads to an increase in the activation energy, which suggests that the lithium-diffusion activation barrier in the spinel-like structure is relatively high for a few of the migration paths, especially when the state of discharge is high. This phenomenon could make Li^+ diffusion in the spinel structure sluggish, and the effect of the surface-layered $LiMnO_2$ structure could be more pronounced. Therefore, we conclude that the highly doped spinel coating containing metal ions such as Al and Mg leads to the formation of monoclinic $LiMnO_2$, which has been shown experimentally and theoretically to have a lower lithium-diffusion activation barrier than that of pristine $LiMn_2O_4$. Thus, the rate performance could be improved in SLMO.

The rate performance of BLMO and SLMO is exhibited in Figure 4a. SLMO retained 90.1 % of its initial capacity at 5C and 87 % at 7C, whereas BLMO retained 80.4 % of its initial capacity at 5C and 72 % at 7C. The high-temperature cycling performance of SLMO is shown in Figure 4b. Its capacity retention per cycle was 99.79; this value is higher than that of BLMO (99.47 % per cycle). After 100 cycles, the capacity retention of BLMO and SLMO was approximately 59 and 82 %, respectively. Furthermore, during a rate-performance test at 24 °C (Figure 4a), the capacity retention of BLMO and SLMO after 30 cycles was approximately 95.15 and 97.91 %, respectively. In general, capacity fading does not occur in oxygen-stoichiometric spinel at room temperature. However, a large decrease in capacity after the fast discharge was observed during the rate-performance test even at room temperature. This decrease in capacity could be attributed to the Jahn–Teller distortion occurring at the surface under nonequilibrium conditions.[21] The Jahn–Teller distortion results in a cubic-to-tetragonal transition, which results in a local strain between the lithiated surface and the host and leads to the collapse of the local microstructure. However, SLMO has a hierarchical atomic structure at the surface, as it shares the ccp oxygen array. Therefore, SLMO experiences a microstrain itself at the surface, which acts as a buffer zone for additional strains during fast discharging. Furthermore, the flat two-cubic-phases reaction of $Li_{0.5}Mn_2O_4$–λ-MnO_2 at 4.11 V were not observed in the case of SLMO. Thus, a sudden change in the lattice parameter could be avoided. For this reason, the collapse of the surface microstructure in SLMO was undermined, and SLMO exhibited an increase in capacity retention of 2.7 %.

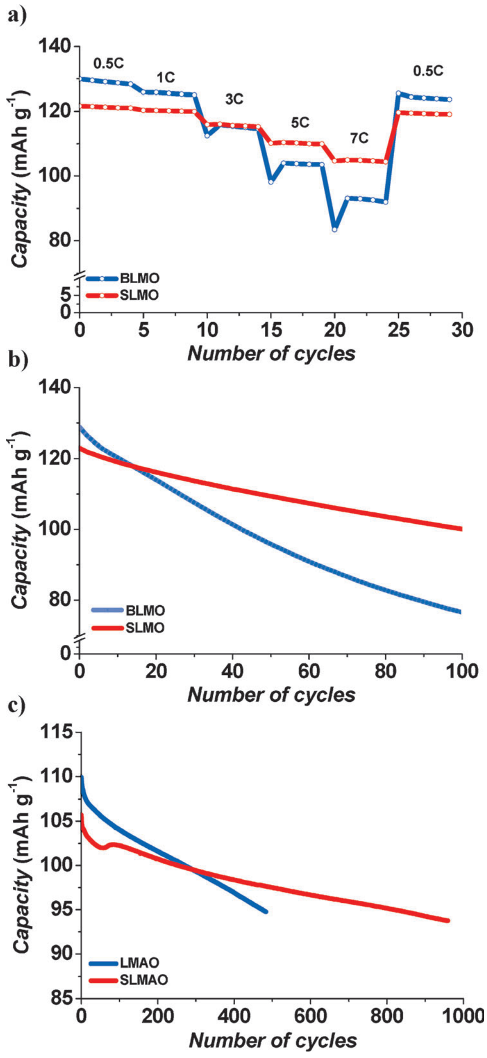

Figure 4. Electrochemical characteristics of BLMO, SLMO, LMAO, and SLMAO. a) Rate capabilities of BLMO and SLMO; the discharge rate performance of BLMO and SLMO was investigated by setting the charge rate to 0.5 C and varying the discharge rate from 0.5 C to 7 C between 3.0 and 4.3 V at 24 °C. 1 C corresponds to the first discharge capacity of the cells. b) Discharge capacity as a function of the number of cycles for BLMO and SLMO at 60 °C; the cells were cycled at charge and discharge rates of 0.5 C and 1 C, respectively. c) Discharge capacity as a function of the number of cycles for SLMAO and LMAO; the cells were cycled at 60 °C with a constant rate of 2 C.

We applied our investigated method to an aluminum-doped spinel, which had a slightly higher capacity than a commercial material. The compositions of the host and coating material were $Li_{1.09}Mn_{1.83}Al_{0.08}O_4$ (LMAO) and $Li_{1.15}Mg_{0.2}Mn_{1.65}O_4$, respectively. A coating of 2 wt % of the bare sample was formed. The spinel-coated LMAO (SLMAO) exhibited structural changes similar to those observed in SLMO after coating; it also exhibited improved electrochemical performance (Figures S13–S21). In particular, the sample retained almost 90 % of its initial capacity after 800 cycles at 60 °C (Figure 4c; see also Figure S21). To the best of our knowledge, such a high cycling performance at 60 °C has never been reported for manganese-based cathode materials, such as 4V spinel or even layered $LiNi_xMn_yCo_zO_2$ (see Figures S22 and S23).

We have demonstrated that a highly doped spinel coating on a stoichiometric spinel cathode material introduces a hierarchical atomic structure at the surface of the host material. STEM analysis showed that the coating layer grew epitaxially on the host material by sharing the ccp oxygen array. However, several structures, including those corresponding to cubic spinel, tetragonal spinel, and monoclinic layered $LiMnO_2$, were observed at the particle surfaces. The effects of the change in the surface microstructure on the electrochemical properties of the host material were investigated through EIS and density functional theory (DFT) calculations. The coated sample, which had a hierarchical structure, exhibited a much lower activation barrier to lithium-ion diffusion than that of the uncoated sample, as supported by the results of the DFT calculations. The coating method improved the electrochemical performance of the host material, including its high-temperature rate capability and cyclability, without resulting in significant capacity reduction. This novel coating method provides insight into the mechanism of surface-microstructure modification for improving the electrochemical performance of cathode materials for LIBs.

Received: September 5, 2014
Revised: November 6, 2014

Keywords: cathodes · epitaxial coating · hierarchical atomic structures · lithium-ion batteries · lithium manganese oxide

---

[1] a) P. G. Bruce, B. Scrosati, J. M. Tarascon, *Angew. Chem. Int. Ed.* **2008**, *47*, 2930–2946; *Angew. Chem.* **2008**, *120*, 2972–2989; b) R. J. Gummow, A. Dekock, M. M. Thackeray, *Solid State Ionics* **1994**, *69*, 59–67; c) M. Yoshio, S. Inoue, M. Hyakutake, G. Piao, H. Nakamura, *J. Power Sources* **1991**, *34*, 147–152.
[2] G. G. Amatucci, N. Pereira, T. Zheng, J. M. Tarascon, *J. Electrochem. Soc.* **2001**, *148*, A171–A182.
[3] a) G. G. Amatucci, C. N. Schmutz, A. Blyr, C. Sigala, A. S. Gozdz, D. Larcher, J. M. Tarascon, *J. Power Sources* **1997**, *69*, 11–25; b) D. H. Jang, Y. J. Shin, S. M. Oh, *J. Electrochem. Soc.* **1996**, *143*, 2204–2211; c) I. H. Cho, S.-S. Kim, S. C. Shin, N.-S. Choi, *Electrochem. Solid-State Lett.* **2010**, *13*, A168–A172.
[4] A. Blyr, C. Sigala, G. Amatucci, D. Guyomard, Y. Chabre, J. M. Tarascon, *J. Electrochem. Soc.* **1998**, *145*, 194–209.
[5] a) J. H. Lee, J. K. Hong, D. H. Jang, Y. K. Sun, S. M. Oh, *J. Power Sources* **2000**, *89*, 7–14; b) Z. H. Zheng, Z. L. Tang, Z. T. Zhang, W. C. Shen, Y. H. Lin, *Solid State Ionics* **2002**, *148*, 317–321.
[6] G. H. Li, H. Ikuta, T. Uchida, M. Wakihara, *J. Electrochem. Soc.* **1996**, *143*, 178–182.
[7] a) B. H. Deng, H. Nakamura, Q. Zhang, M. Yoshio, Y. Y. Xia, *Electrochim. Acta* **2004**, *49*, 1823–1830; b) N. Hayashi, H. Ikuta, M. Wakihara, *J. Electrochem. Soc.* **1999**, *146*, 1351–1354.
[8] Q. M. Zhong, A. Bonakdarpour, M. J. Zhang, Y. Gao, J. R. Dahn, *J. Electrochem. Soc.* **1997**, *144*, 205–213.
[9] a) B. J. Hwang, R. Santhanam, D. G. Liu, Y. W. Tsai, *J. Power Sources* **2001**, *102*, 326–331; b) S. T. Myung, S. Komaba, N. Kumagai, *J. Electrochem. Soc.* **2001**, *148*, A482–A489.
[10] J. Cho, T.-J. Kim, Y. J. Kim, B. Park, *Chem. Commun.* **2001**, 1074–1075.
[11] a) W.-K. Kim, D.-W. Han, W.-H. Ryu, S.-J. Lim, H.-S. Kwon, *Electrochim. Acta* **2012**, *71*, 17–21; b) J. Cho, Y. J. Kim, T. J. Kim, B. Park, *J. Electrochem. Soc.* **2002**, *149*, A127–A132.
[12] Y. K. Sun, Y. S. Lee, M. Yoshio, K. Amine, *Electrochem. Solid-State Lett.* **2002**, *5*, A99–A102.
[13] J. S. Gnanaraj, V. G. Pol, A. Gedanken, D. Aurbach, *Electrochem. Commun.* **2003**, *5*, 940–945.
[14] D. Arumugam, G. P. Kalaignan, *J. Electroanal. Chem.* **2008**, *624*, 197–204.
[15] S. Lee, M. Jeong, J. Cho, *Adv. Energy Mater.* **2013**, *3*, 1623–1629.
[16] a) Z. Chen, Y. Qin, K. Amine, Y. K. Sun, *J. Mater. Chem.* **2010**, *20*, 7606–7612; b) M.-J. Lee, S. Lee, P. Oh, Y. Kim, J. Cho, *Nano Lett.* **2014**, *14*, 993–999; c) K. T. Lee, S. Jeong, J. Cho, *Acc. Chem. Res.* **2012**, *46*, 1161–1170; d) J. Cho, Y. J. Kim, B. Park, *Chem. Mater.* **2000**, *12*, 3788–3791.
[17] Z. Chen, J. R. Dahn, *Electrochem. Solid-State Lett.* **2003**, *6*, A221–A224.
[18] T. Ohzuku, M. Kitagawa, T. Hirai, *J. Electrochem. Soc.* **1990**, *137*, 769–775.
[19] S. K. Mishra, G. Ceder, *Phys. Rev. B* **1999**, *59*, 6120–6130.
[20] a) B. Xu, S. Meng, *J. Power Sources* **2010**, *195*, 4971–4976; b) M. Nakayama, M. Kaneko, M. Wakihara, *Phys. Chem. Chem. Phys.* **2012**, *14*, 13963–13970.
[21] M. M. Thackeray, Y. Shao-Horn, A. J. Kahaian, K. D. Kepler, E. Skinner, J. T. Vaughey, S. A. Hackney, *Electrochem. Solid-State Lett.* **1998**, *1*, 7–9.